International Journal of Biological Macromolecules 254 (2024) 127775

Contents lists available at ScienceDirect

International Journal of Biological Macromolecules

journal homepage: www.elsevier.com/locate/ijbiomac

Structural insights and aggregation propensity of a super-stable monellin mutant: A new potential building block for protein-based nanostructured materials

Rosanna Lucignano [a], Roberta Spadaccini [b], Antonello Merlino [a], Diletta Ami [c], Antonino Natalello [c], Giarita Ferraro [a,*], Delia Picone [a,*]

[a] Department of Chemical Sciences, University of Naples Federico II, Complesso Universitario di Monte Sant'Angelo, Via Cintia, 80126 Naples, Italy
[b] Department of Science and Technology, University of Sannio, Via de Sanctis, 82100 Benevento, Italy
[c] Department of Biotechnology and Biosciences, University of Milano-Bicocca, Piazza della Scienza, 20126 Milano, Italy

ARTICLE INFO

Keywords:
Protein aggregation
Functional amyloids
MNEI
Mut9
Protein structure
Nanostructured biomaterials

ABSTRACT

Protein fibrillation is commonly associated with pathologic amyloidosis. However, under appropriate conditions several proteins form fibrillar structures *in vitro* that can be used for biotechnological applications. MNEI and its variants, firstly designed as single chain derivatives of the sweet protein monellin, are also useful models for protein fibrillary aggregation studies. In this work, we have drawn attention to a protein dubbed Mut9, already characterized as a "super stable" MNEI variant. Comparative analysis of the respective X-ray structures revealed how the substitutions present in Mut9 eliminate several unfavorable interactions and stabilize the global structure. Molecular dynamic predictions confirmed the presence of a hydrogen-bonds network in Mut9 which increases its stability, especially at neutral pH. Thioflavin-T (ThT) binding assays and Fourier transform infrared (FTIR) spectroscopy indicated that the aggregation process occurs both at acidic and neutral pH, with and without addition of NaCl, even if with a different kinetics. Accordingly, Transmission Electron Microscopy (TEM) showed a fibrillar organization of the aggregates in all the tested conditions, albeit with some differences in the quantity and in the morphology of the fibrils. Our data underline the great potential of Mut9, which combines great stability in solution with the versatile conversion into nanostructured biomaterials.

1. Introduction

The protein fibrillar aggregation mechanism has been often [1] studied with reference to several human diseases that are characterized by the formation of amyloid deposits [2,3]. However, it has been widely demonstrated that a huge number of proteins, unrelated to any known disease, can form amyloid structures *in vitro* under appropriate conditions [4]. In fact, self-assembling proteins became popular not only for their implication in pathological conditions, but also for their potential as building blocks to obtain protein-based nanomaterials with attracting potential applications, such as targeted drug delivery systems for cancer therapy or diagnostic tools or vaccine development [5]. Protein-based nanomaterials present several advantages, such as sustainable and scalable production, long-term stability, and absence of immunogenicity [6,7].

The ability of proteins to self-assemble forming fibrils is an intricate process and is influenced by different parameters, intrinsic or extrinsic to the protein. Extrinsic factors include physico-chemical parameters, such as pH, temperature, ionic strength and protein concentration [8–10], while the intrinsic factors refer to the specific features of the protein, such as charge, hydrophobicity, patterns of polar and non-polar residues, and also propensity to adopt different secondary structure motifs. In a globular protein the polypeptide main chain and the hydrophobic side chains are largely buried within the folded structure. When they become exposed, for example when the protein is partly unfolded, the conversion of protein molecules into aggregated structures has a higher probability to occur [11]. Fibrillar aggregation is generally characterized by a lag phase, followed by a period of rapid growth, and seems to involve the formation of soluble oligomers [12,13].

Specific regions of the protein, known as aggregation-prone regions,

* Corresponding authors at: Department of Chemical Sciences, University of Naples Federico II, Complesso Universitario di Monte Sant'Angelo, via Cintia, 21, 80126 Naples, Italy.
E-mail addresses: giarita.ferraro@unina.it (G. Ferraro), picone@unina.it (D. Picone).

https://doi.org/10.1016/j.ijbiomac.2023.127775
Received 28 August 2023; Received in revised form 12 October 2023; Accepted 27 October 2023
Available online 30 October 2023

may have a central role in the formation of stable fibrillar aggregates [14,15]. The identification of such regions could drive the design of protein mutants able to form ordered intermolecular assemblies that can be easily isolated, replicated and used for potential biotechnological applications.

In this framework we have undertaken an investigation of the aggregation process of MNEI, a single chain derivative of the sweet plant protein monellin designed by linking the two monellin chains through a Gly-Phe dipeptide linker. The resulting protein retained the same sweetness of the parent protein but displayed a higher thermal stability [16]. Besides its potential as protein-based sweetener, this globular protein also represents a good model for protein folding, unfolding and self-assembly studies. Indeed, the folding and unfolding processes of MNEI have been deeply characterized [17–19] and appear to be multi-state, with parallel pathways populated by multiple intermediates [18]. Jha and coworkers demonstrated that MNEI unfolding process initiates with the protein expansion into a dry molten globular state in which the single α-helix moves out from the native state gradually [20]. It has been recently reported a systematic study of the aggregation mechanisms of this protein showing that MNEI, under mild denaturing conditions/early unfolding stages, can be converted into insoluble, amyloid state, giving rice to linear or branched structures. All these structures can be observed at acidic pH (pH = 2.5), where the prolonged incubation of the protein, at a temperature below its melting temperature, prompts the formation of aggregates with the typical features of amyloid fibrils. On the contrary, at neutral pH (pH = 6.8), only amorphous aggregates can be detected [21], suggesting that pH is the main switch between amyloid and amorphous aggregation [22]. Furthermore, the presence of salts, particularly chlorides, accelerates fibrils formation [23]. Due to its great potential, many studies have been conducted to improve MNEI features. Indeed, site-directed mutagenesis has been used as a tool for the rational design of mutants with greater resistance and higher thermal and chemical stability, even at neutral pH. Liu and co-workers pointed out that many mutants, able to enhance the thermostability of the protein, were distributed at the two ends of α-helix [24]. They showed how the replacement of the unpartnered ionizable residue Glu23 from the hydrophobic core of the protein with an alanine (E23A) can stabilize the native state of the protein. In addition, they proved that C41 residue, located at the second β-strand, can contribute to thermostability improvement playing a concerted role with E23 to account for the pH-dependent stability of the protein at pH > 8 [24]. Esposito et al. designed and produced Y65R-MNEI, a mutant significantly sweeter than the parent protein, predicted to interact more efficiently with the sweet receptor T1R2:T1R3 [25], while keeping the same aggregation propensity of MNEI [21].

Based on these findings, recently we have designed a new mutant, Mut9, selecting the most promising point mutations: Y65R, E23A, C41A and S76Y [26]. Mut9 showed high stability in acidic and neutral environments, a higher melting temperature (over 20 °C) than that of MNEI and resulted twice sweeter than MNEI. Notably, it preserved its structure and function even after 10 min boiling, particularly at pH 6.8, and after 6-months of shelf-life in different conditions. This protein is the proof that multiple mutations of different residues can lead to an additive performance with both improved sweetness and stability, suggesting that the sweetness and stability could be modulated by independent molecular mechanisms.

Inspired by these features, in this paper we have addressed a comparative study between MNEI and Mut9 to understand the structural grounds of the higher stability of the latter protein and investigate its amyloid aggregation propensity. The analysis of the effect of single point mutations on Mut9 stability has been evaluated by means of X-ray crystallography coupled to molecular dynamic predictions. In addition, we have evaluated Mut9 aggregation tendency at two different pHs and compared the morphology of the obtained fibrils. Specifically, we have studied the kinetics of aggregation, in different experimental conditions, by using the ThT assay and FTIR spectroscopy, and we have analyzed fibrils morphology by TEM.

2. Materials and methods

2.1. Expression and purification of MNEI and Mut9

MNEI and Mut9 were expressed in *Escherichia coli* BL21(DE3) and purified from the cell lysate by ion-exchange chromatography followed by size-exclusion chromatography as previously described [26].

2.2. Crystallization, X-ray diffraction data collection, structure solution and refinement

MNEI and Mut9 were crystalized at 293 K by hanging drop vapor diffusion and a reservoir solution containing 30–33 % PEG4K, 0.1 M sodium acetate buffer pH 4.5 and 0.2 M ammonium sulfate mixing 1 μL protein (4.5 and 5.7 mg mL^{-1} in 5.0 mM HCl, respectively) with 1 μL mother liquor at 20 °C. Crystals grew within one week (Fig. S6). X-ray diffraction data were collected at 100 K on a Pilatus detector at XRD2 beamline of Elettra synchrotron, Trieste, Italy. Data collection statistics are reported in Table S7. Data were processed and scaled in $P12_11$ space group using AutoPROC [27]. Phase problem was solved by molecular replacement method using as starting model the structure from protein data bank (PDB) (2O9U). Refinement was carried out using Refmac-CCP4i [28] and model building using Coot [29]. Refinement statistics are reported in Table S7. Coordinates and structure factors have been deposited in the protein data bank under the accession codes 8Q0S and 8Q0R, respectively.

2.3. ThT binding assay

MNEI at a concentration of 216 μM was incubated in 20 mM phosphate buffer at pH 2.5, while Mut9, at the same concentration, was incubated in 20 mM phosphate buffer at pH 2.5 and 6.8 either with or without 150 mM NaCl. The aggregation kinetics was followed recording time points. Thioflavin T (ThT) stock solution of 1 mM was prepared dissolving ThT powered in 20 mM phosphate buffer pH 6.8. Samples at different time points were prepared by adding 19 μL of protein samples (final protein concentration 10 μM) and 12 μL of ThT stock solution (final concentration 30 μM) in 20 mM phosphate buffer pH 6.8 to a final volume of 400 μL. Fluorescence emission spectra were recorded on a HORIBA Fluoromax-4 in the range of 400–600 nm with scan speed of 100 nm/min, upon excitation at 440 nm. Excitation and emission slits were both set at 5 nm. Fluorescence intensity values at 485 nm emission were plotted as a function of time. The reported values represent the average of three independent experiments.

2.4. Transmission electron microscopy (TEM) analysis

Aliquots of the protein solution were taken and diluted 50 times with deionized water. 3 μL drops of the samples were deposited for 3 min on a carbon-coated copper TEM grid (200 mesh) and then, the excess fluid was drained off with filter paper and air-dried. Average fibril thickness was calculated from TEM images using IMAGE J (*ImageJ* (*nih.gov*)). The images were collected using a FEI TECNAI G2 S-twin apparatus operating at 120 kV (LaB_6 source).

2.5. FTIR spectroscopy

FTIR measurements in attenuated total reflection (ATR) mode were performed in the mid-IR range as previously described [22,30]. In particular, 2 μL of the samples were deposited on the single reflection diamond crystal of the ATR device (Quest, Specac) and dried at room temperature before the collection of the ATR-FTIR spectra by the Varian 670-IR spectrometer (Varian Australia Pty Ltd.). The following parameters were employed: spectral resolution of 2 cm^{-1}, scan speed of 25

kHz, 1024 scan coadditions, and nitrogen-cooled Mercury Cadmium Telluride detector. After 48 h of incubation, samples were centrifuged at 16,000 rcf for 30 min and the ATR-FTIR spectra of the pellets were collected as described above. Absorption spectra were smoothed using the Savitsky-Golay method before the second derivative analysis. Spectral collection and analysis were performed with the Resolutions-Pro software (Varian Australia Pty Ltd., Mulgrave VIC, Australia).

2.6. Molecular dynamics simulations

Crystal structures of MNEI (8Q0S) and Mut9 (8Q0R) were used for Molecular dynamics simulations. Alle the calculations were performed with the Amber20 suite [31] using the ff14sb force field for the proteins, pKa values of ionizable residues of the two proteins were estimated by H++ at pH 2.5 and pH 7.0 [32]. Each system was stepwise pre-equilibrated at 300 K with 2 fs steps for 2 ns and run for further 100 ns as a pre-production step. Simulations were conducted under NPT conditions of constant temperature (300 K or 350 K) and pressure (1 atm); Berendsen thermostat was used to maintain the constant temperature. The SHAKE algorithm was employed to constrain bonds involving any hydrogen atoms. Periodic boundary conditions were employed to calculate non-bonded interactions using a 10 Å cut-off distance. The Particle Mesh Ewald (PME) method was used to calculate electrostatic interactions. Subsequent 100 ns trajectories were processed and evaluated in Jupyter Notebook using PYTRAJ and CPPTRAJ [33] and NGLview [34]. For each condition were generated three independent simulations. The secondary structure variation was calculated using the AMBER DSSP algorithm.

3. Results

3.1. X-ray structures of MNEI and Mut9

The structures of MNEI and Mut9 from isomorphic crystals possess 2032 and 1976 atoms, respectively. The X-ray structures (Fig. 1), obtained from crystals with two molecules in the asymmetric unit (chain A and chain B), have been refined at a resolution of 1.19 and 1.50 Å, and to R-factor and Rfree values within the range 0.218/0.256 and 0.223/0.274, respectively.

Both structures are very similar to each other, as revealed by the analysis of the values of the root mean square deviations of the distances between the Cα (RMSD, Table S1), and to the structures of MNEI and its mutants reported in literature (Table S2). In fact, the graphs of B-relative (obtained by normalization of B-factors [35] reported as a function of residue of MNEI and Mut9 (Fig. S1) are very similar, except for the region between residues 45–60, where Mut9 shows higher B-relative values than MNEI. This difference could be related to the L23 loop located in this region (residues 47–56) which, in all the structures reported for MNEI and its derivatives, is generally highly flexible or disordered. Indeed, in the structure of Mut9 the electron density map in this region is not well defined.

To understand the determinants of the different thermal stability of MNEI and Mut9, the structural features of each molecule of the asymmetric unit were analyzed and compared. MNEI and Mut9 possess a comparable number of hydrogen bonds and salt bridges, similar solvent-accessible surfaces and hidden regions, and similar volume (Table S3). Thus, the two proteins show similar structural features, suggesting that the presence of the mutation sites do not introduce variations of general protein conformation, as also suggested by their capability to recognize the same receptors, eliciting the sweet taste. Therefore, we have analyzed one by one the single point mutations to investigate the reasons for the increased Mut9 stability with respect to MNEI.

3.2. Analysis of the effects of single point mutations

3.2.1. Y65R mutation

The mutation Y65R introduces a positive charge on the surface of MNEI associated with a sweetness increase [36] and a thermal stability decrease of the protein [21]. Crystallographic studies revealed that the mutation induces structural changes in the C-terminal region of the protein, responsible for the lower stability of Y65R mutant to the respect of MNEI [21]. In particular, the Arg65 side chain in Y65R mutant appears disordered. The disorder of this residue affects the conformation of the residue Tyr63, which, in the structure of MNEI, interacts with the residue Phe94 at the C-terminus. Consequently, in the Y65R mutant, the distances between Tyr63 and Phe94 are slightly greater than those observed in MNEI [21]. This difference could contribute to the lower thermal stability of the mutant compared to that of MNEI. In contrast, in the two chains of the asymmetric unit of MNEI and Mut9, the electron density map of residue 65 is well defined (Fig. S2). The analysis of the distances between residues 63 and 94 shows that the neighborhood of residue 65 in Mut9 is more similar to MNEI than to Y65R, suggesting that in this mutant the Y65R mutation is less destabilizing than in Y65R-MNEI (Table S4, Fig. 2).

3.2.2. C41A mutation

The C41A mutation is related to the sweetness decrease and the thermal stability increase of MNEI [24]. This residue is located in a hydrophobic pocket formed by residues Ile6, Thr12, Leu15, Val37 and Leu62. In both molecules of the asymmetric unit of MNEI crystals, the

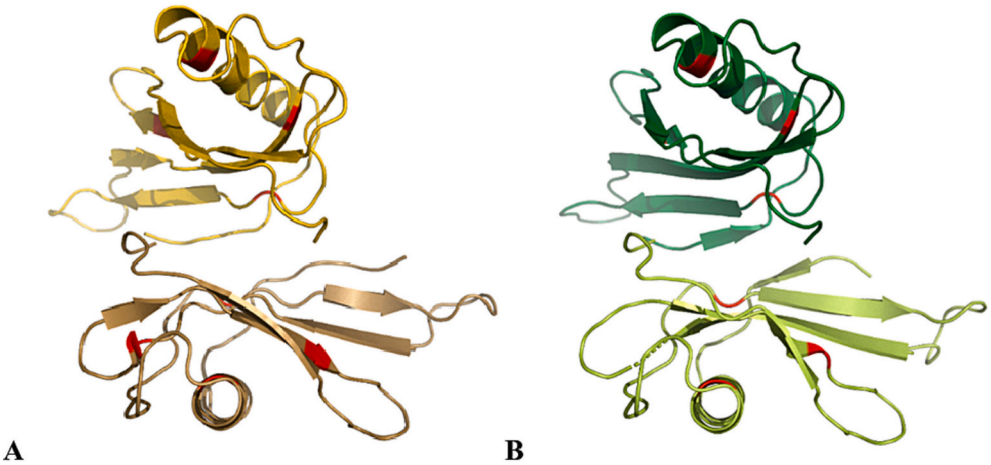

Fig. 1. Cartoon representation of the X-ray structures of MNEI (A) and Mut9 (B). The two molecules of the asymmetric unit are shown in dark yellow and gold for MNEI and in light and dark green for Mut9. The position of the mutated residues is indicated in red.

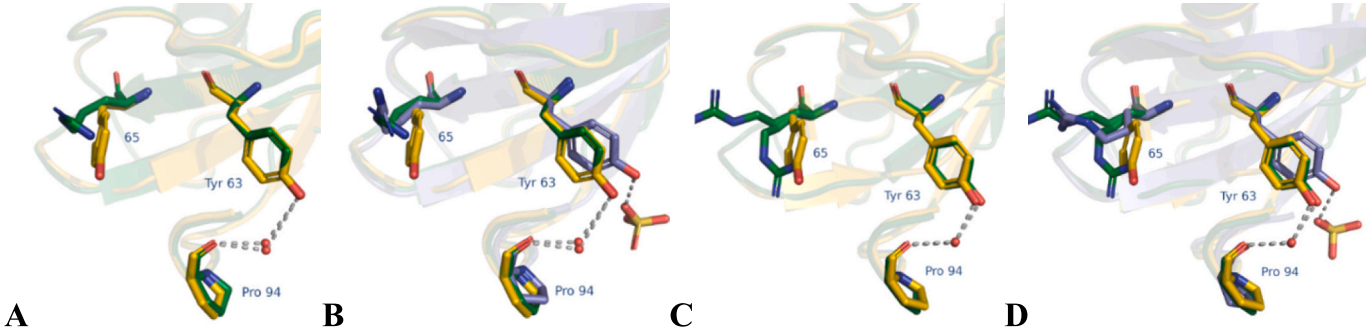

Fig. 2. Neighborhood of residue 65. The interactions of residues 63 and 94, which have been hypothesized to play an important role in protein stability, are highlighted. In yellow MNEI, in green Mut9 and in blue Y65R. Chains A in panels A and B, chains B in panels C and D.

sulfur atom of Cys41 forms unfavorable interactions with the residues of this pocket. In Mut9 the C41A substitution eliminates the unfavorable MNEI-Cys41 interactions, thus stabilizing the structure of the mutant. In fact, the side chain of the alanine is less bulky than that of cysteine. In this way the surrounding residues have much more space. The comparison between the structures of MNEI and Mut9 also shows a conformational change of Leu62 side chain due to the mutation. Leu62 occupies part of the empty space introduced by the C → A substitution (Fig. 3).

This conformational variation is observed in both molecules of the asymmetric unit. In the two chains of the asymmetric unit of MNEI and Mut9, the electron density map of residue 41 is well defined (Fig. S3). Details of the distances between residues 41 and 62 are reported in Table S5.

3.2.3. *E23A mutation*

The E23A mutation is related to a strong increase in thermal stability [37]. pH plays an important role in modulating the stability of MNEI and its mutants. It has been demonstrated that residue E23, buried in a hydrophobic pocket of the protein at one end of the alpha helix, is responsible for a pH dependent stability of the protein, due to its anomalous pKa. In the two chains of the asymmetric unit of MNEI and Mut9, the electron density map of residue 23 is well defined (Fig. S4). MNEI structure, notably, shows that the Glu23 side chain is in contact with the residues Ile26, Phe89, Leu86, Tyr29 e Gln28 (Fig. 4) in both molecules of the asymmetric unit, but these interactions are energetically unfavorable. The substitution E23A in Mut9 removes these unfavorable interactions and introduces an empty space around residue 23, which is partly occupied by small displacements of the residues of the hydrophobic pocket.

The comparison of the distances between Phe89 and A/Glu23 residues are reported in Table S6. This could contribute to the increased stability of Mut9 with respect to MNEI.

3.2.4. *S76Y mutation*

Residue 76 is located within the β3 sheet of the protein. Literature results demonstrate that replacing Ser76 with Tyr increases the stability of the protein [38]. Residue 76 is well defined in the electron density maps of MNEI and Mut9 (Fig. S5). In the two molecules of MNEI structure, serine forms an unfavorable interaction with the Lys85 atoms and a hydrogen bond with a water molecule (Fig. 5). In the Mut9 structure, the tyrosine side chain forms a hydrogen bond with the carbonyl oxygen of Lys56 and with the side chain of Asp78, although in one of the two molecules of the asymmetric unit this interaction is mediated by the presence of a water molecule (Fig. 5). Tyr76 side chain forms van der Waals interactions with carbon atoms of the residues Ile46, Lys56, Lys85 and Leu87, which are in its neighborhood. All these interactions can make an important contribution in increasing the stability of the mutant with respect to MNEI.

The punctual analysis of the additional interactions in Mut9 accounts for the increased thermal stability observed for the protein with respect to the parent MNEI both at acidic and neutral pH [26]. Indeed, the network of stabilizing interactions located in different protein areas counteracts the 4–8 degrees decrease of the melting temperature associated to the mutation Y65R [21], due to the increased distances between residues Tyr63 and Phe94.

3.3. *Aggregation propensity*

The aggregation tendency of Mut9 was studied by standard ThT fluorescence assay and compared with literature data reported for MNEI [21]. The protein was incubated, with and without NaCl, at pH 2.5 and

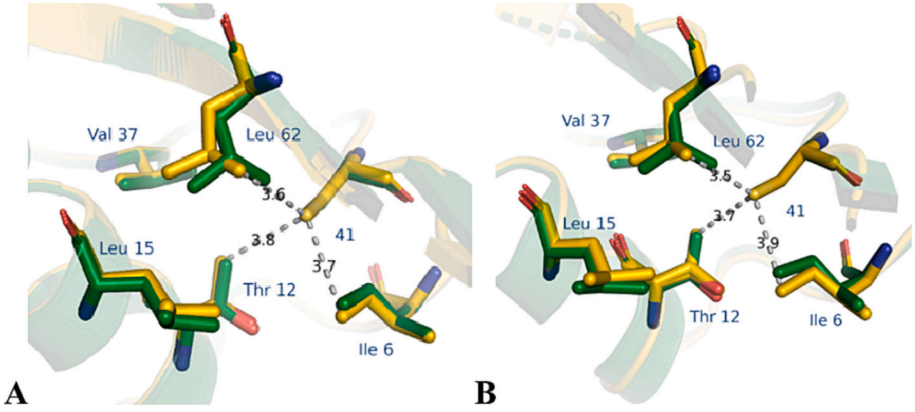

Fig. 3. Details of the interactions of residue 41 with the surrounding residues in the structures of MNEI (yellow) and Mut9 (green). Chains A are reported in panel A, chains B in panel B. The distances are represented by grey dashes.

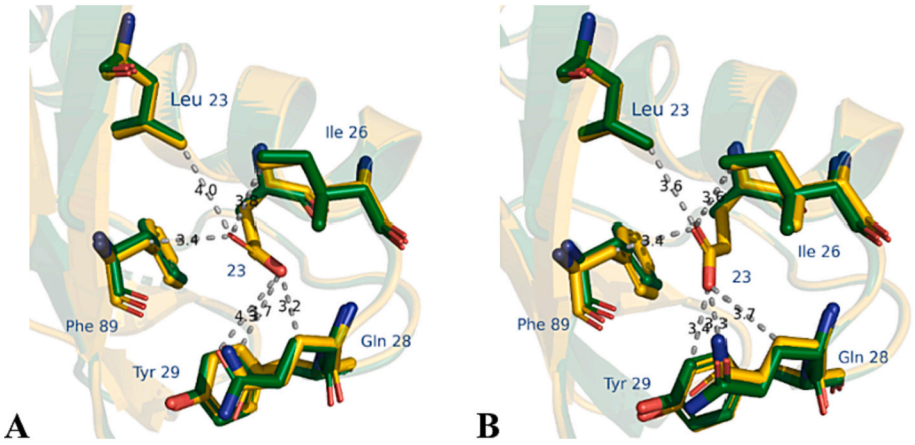

Fig. 4. Details of the interactions of residue 23 with the surrounding residues in the structures of MNEI (yellow) and Mut9 (green). Chains A are reported in panel A, chains B in panel B. The distances are represented by grey dashes.

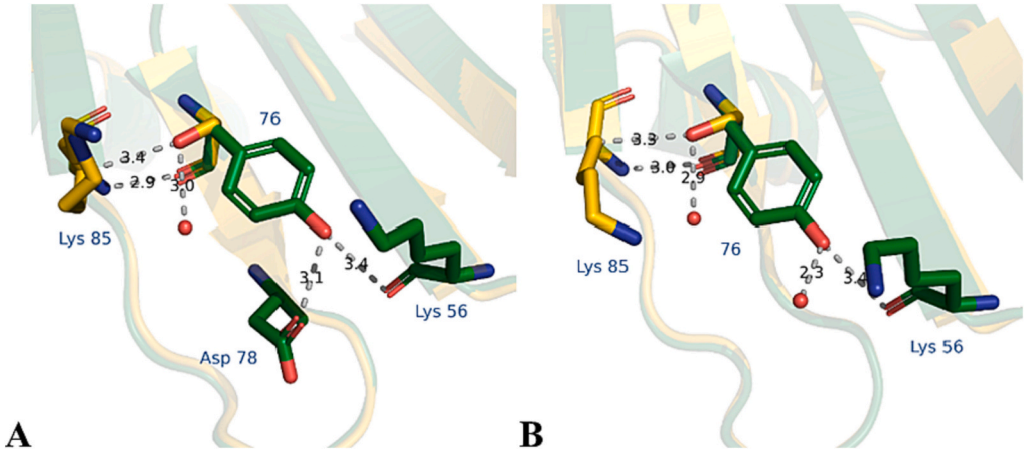

Fig. 5. Details of the interactions of residue 76 with the surrounding residues in the structures of MNEI (yellow) and Mut9 (green). Chains A are reported in panel A, chains B in panel B. The distances are represented by grey dashes.

6.8, at 75 and 90 °C, respectively, *i.e.*, in temperature conditions corresponding to the early unfolding steps, according to the thermal denaturation study previously reported [26]. Indeed, it has been shown that partial protein unfolding is a preliminary step in the formation of amyloid-like protein fibrils [39]. The aggregation kinetics was followed for two days, for pH 6.8, and for four days, for pH 2.5, monitoring the ThT fluorescence signal until a stationary phase was reached (Fig. 6A). The data reported in Fig. 6 indicated that ThT fluorescence intensity increases as function of time for all the analyzed samples, but the pH drastically influences ThT binding. Particularly, i) at neutral pH, the signal reached the plateau after only one day of incubation, and the intensity is lower in comparison with the one obtained at acidic pH; ii) at pH 2.5, the *plateau* was reached after two days of incubation. The curves from all the samples show a sigmoidal line-shape, more evident at acidic pH, as expected for amyloid fibrils formation mechanism, which involves three phases, *i.e.*, lag, elongation, and *plateau* [39]. Interestingly, at both pHs, the aggregation process occurs also without NaCl. Nevertheless, the ionic strength affects the kinetic in an opposite way in these two conditions. In fact, at acidic pH the kinetic in the presence of NaCl is faster than that in the absence of NaCl, while, at neutral pH, the ionic strength delays the kinetics. Anyway, quite a high response to ThT assay, under all conditions, suggests the possible presence of fibrillar aggregates. To investigate the morphology of the aggregates formed by Mut9, aliquots of the samples incubated for two days at neutral pH and for four days at acidic pH were analyzed by TEM. Representative images of the samples obtained under all conditions tested are reported in Fig. 6 (from B to E). Differently from MNEI, Mut9 aggregates showed a fibrillar organization at both acidic and neutral pH, independently on the presence of NaCl. However, the quantity and the morphology of the fibrils are influenced by NaCl at both pHs, reflecting the different ThT fluorescence intensity. In fact, at pH 2.5, in the presence of NaCl the ThT emission is much more intense, suggesting the presence of a higher number of amyloid fibrils. This hypothesis is confirmed by TEM. In fact, as observed in Fig. 6C, there are more fibrils, and they are more branched in comparison to the fibrils of the sample without salt (Fig. 6B). On average, the fibrils formed in the presence of sodium chloride have a diameter of 23 ± 2 nm or, if branched, of 14 ± 1 nm, while in the absence of salt show a width of 21 ± 1 nm. In both cases, *i.e.*, in the absence or in the presence of NaCl, the length of fibrils is about 4 ± 1 μm. On the other hand, at pH 6.8, in the absence and in the presence of NaCl only few, very long fibrils, can be detected. In fact, as suggested by ThT binding assays, the fluorescence intensity is much lower than that observed at acidic pH. Moreover, on the contrary of what occurs at pH 2.5, in this case the fluorescence intensity in the absence of NaCl is slightly higher than in presence of salt, and the fibrils are more branched than those obtained in the presence of NaCl (Fig. 6D-E).

Regarding fibrils dimensions, in both the analyzed cases there is a coexistence of fibrils formed by a single filament (13 ± 2 nm) and fibrils formed by two filaments (23 ± 1 nm). Also in these experimental conditions, the obtained fibrils show a length of about 3 ± 1 μm.

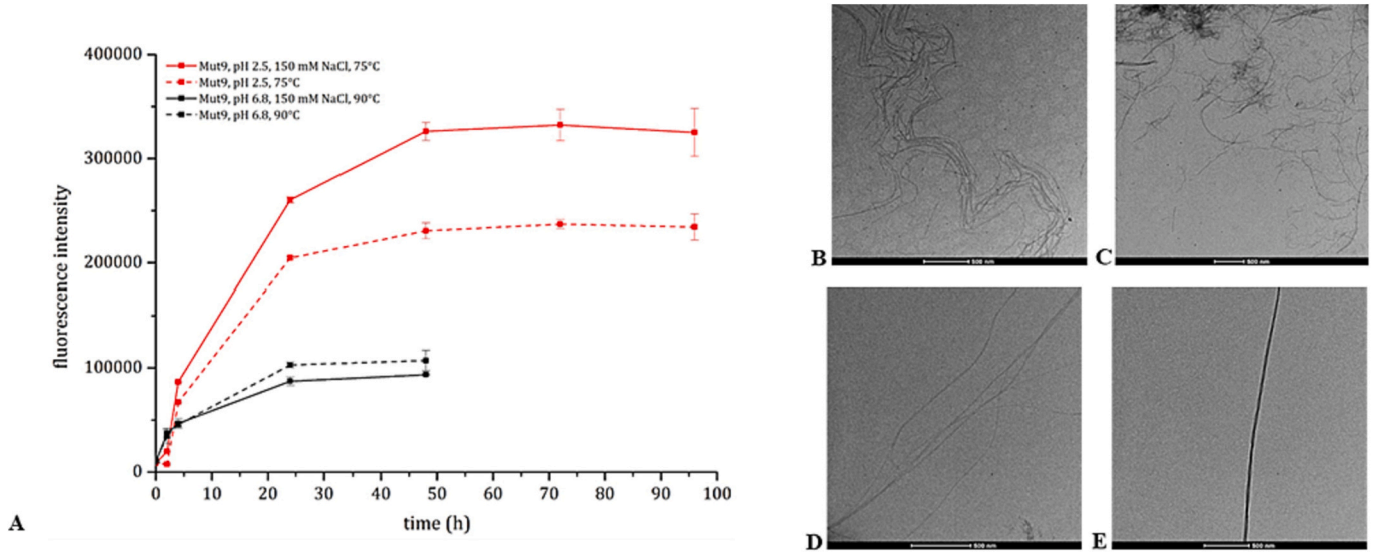

Fig. 6. ThT binding assay of Mut9 (panel A). Fluorescence intensity values are reported as function of time for: Mut9, pH 2.5, NaCl, 75 °C (solid red line), Mut9, pH 2.5, 75 °C (dotted red line), Mut9, pH 6.8, NaCl, 90 °C (solid black line) and Mut9, pH 6.8, 90 °C (dotted black line). Transmission electron images of Mut9 (panels B-E). Samples incubated in 20 mM phosphate buffer pH 2.5 at 75 °C after 96 h without (B) and with (C) 150 mM sodium chloride, and in 20 mM phosphate buffer pH 6.8 at 90 °C after 48 h without (D) and with (E) 150 mM of sodium chloride. The samples were observed without any staining procedure; therefore, protein fibrils appear darker with respect to the background. The scale bars are 500 nm.

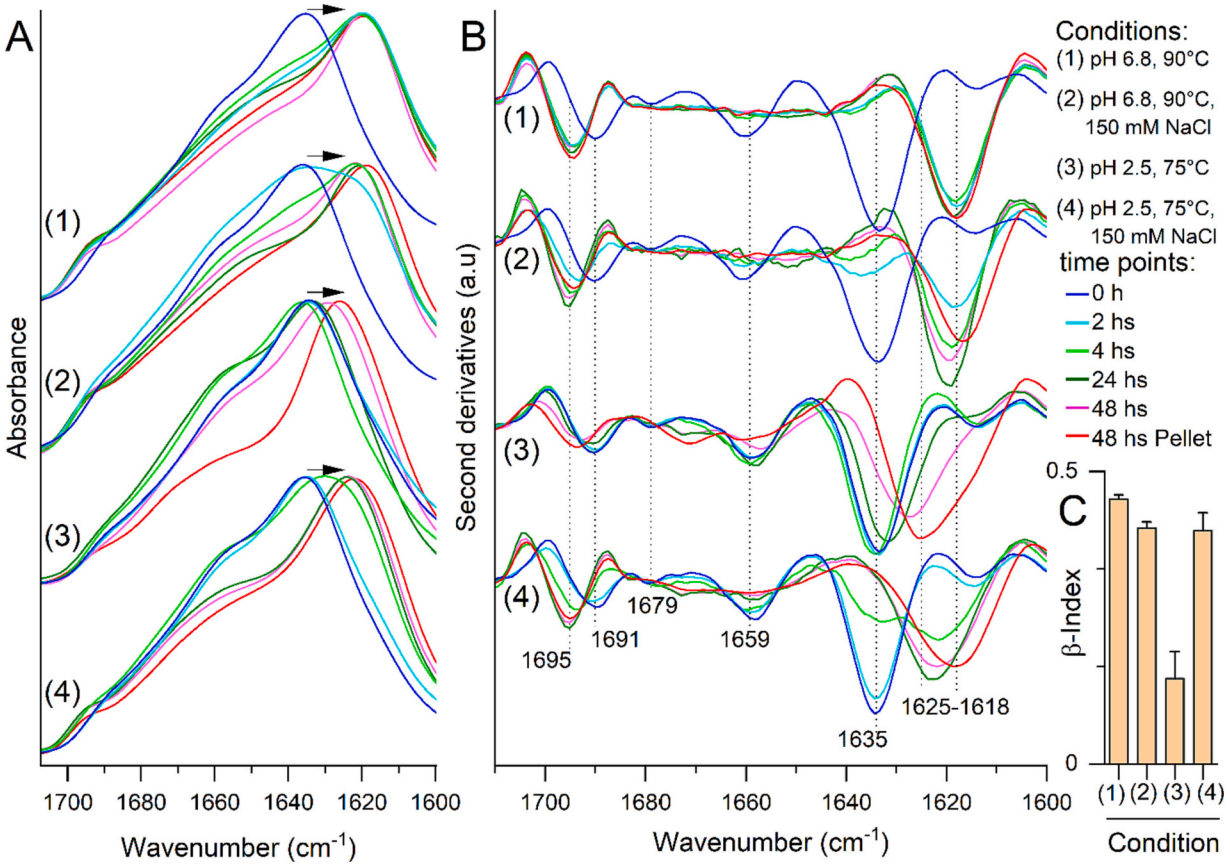

Fig. 7. Mut9 aggregation characterized by FTIR spectroscopy. A, B) Absorption and second derivative spectra of Mut9 incubated under different conditions, specified as (1) to (4), for different times, as indicated. After 48 h of incubation, the spectra of the pellet were also collected. Arrows point to the observed changes of the Amide maximum. The main peak positions are shown. C) The β-index of the final aggregates is evaluated from the intensities of the second derivative spectra of the pellets. In particular, the ratio of the ~1695 cm^{-1} peak intensity to that of the maximum peak between 1625 and 1618 cm^{-1} was reported. Error bars represent the standard deviations of at least three measurements.

3.4. Fourier transformed infrared spectroscopy

The presence of fibrillary aggregates was also investigated by FTIR spectroscopy, which allows to detect the presence of intermolecular β-sheet structures, universally accepted hallmarks of amyloid aggregates [40].The aggregation kinetics of Mut9 incubated under different conditions, *i.e.* at pH 2.5 and at pH 6.8, both in the absence and in the presence of NaCl, is reported in Fig. 7. At the beginning of incubations (time 0 h), the second derivative spectra of Mut9 (Fig. 7B) display, in all the reported conditions, the following peaks that were assigned to the secondary structures of the native protein, in agreement with our previous works [22,30]: ~1635 cm^{-1} and ~1691 cm^{-1}, due to intramolecular β-sheets; ~1659 cm^{-1}, mainly due to α-helices, with contribution of random coils; ~1679 cm^{-1}, assigned to β-turns. During incubation, a downshift of the main Amide *I* peak is observed in all the absorption spectra (Fig. 7A) with a dissimilar kinetics in the different conditions. As shown in the second derivative spectra (Fig. 7B), in the samples incubated at pH 6.8 and 90 °C, the components assigned to the native protein structures completely disappear already after 2 and 4 h in the absence and in the presence of NaCl, respectively. Moreover, two new peaks at around 1695 cm^{-1} and ~1618 cm^{-1} appear. These components are unequivocally assigned to the formation of intermolecular β-sheet structures typical of protein aggregates. In the samples incubated at pH 2.5 and 75 °C, starting from 24 h the ~1635 cm^{-1} peak assigned to the native protein structures downshifts to ~1625 cm^{-1}, while the ~1691 cm^{-1} peak upshifts to ~1695 cm^{-1}. In the samples incubated at pH 2.5, 150 mM NaCl, the IR response of the native structure disappears between 4 and 24 h, and new components at ~1695 cm^{-1} and between 1625 and 1618 cm^{-1} arise, which can be assigned to the β-sheet structures of the protein aggregates (Fig. 7B). The second derivative spectra of the protein pellets collected after 48 h of incubation display similar spectral features for the samples at pH 6.8 and 90 °C in the presence and absence of 150 mM NaCl and for the sample at pH 2.5, 150 mM NaCl at 75 °C. The sample at pH 2.5 and 75 °C displays a different position of the main Amide *I* peak and a reduced intensity of the ~1695 cm^{-1} peak. For a quantitative comparison, the β-index was evaluated from the second derivative spectra. This index is related to the orientation of the β-strands and it was suggested that it is proportional to the percentage of anti-parallel *vs.* parallel organization of the β-strands [41]. A lower β-index value (Fig. 7C) was obtained for the sample at pH 2.5 and 75 °C, indicating differences in the internal structures of this aggregates compared to those obtained under the other conditions. In particular, the lower value of the β-index might suggest a higher presence of parallel β-sheet structures in the final aggregates [41]. Moreover, the absorption spectrum of the final aggregates obtained at pH 2.5 and 75 °C displays a lower absorption around 1660 cm^{-1} (Fig. 7A), indicating a lower content of disordered structures compared to the aggregates obtained in the other tested conditions.

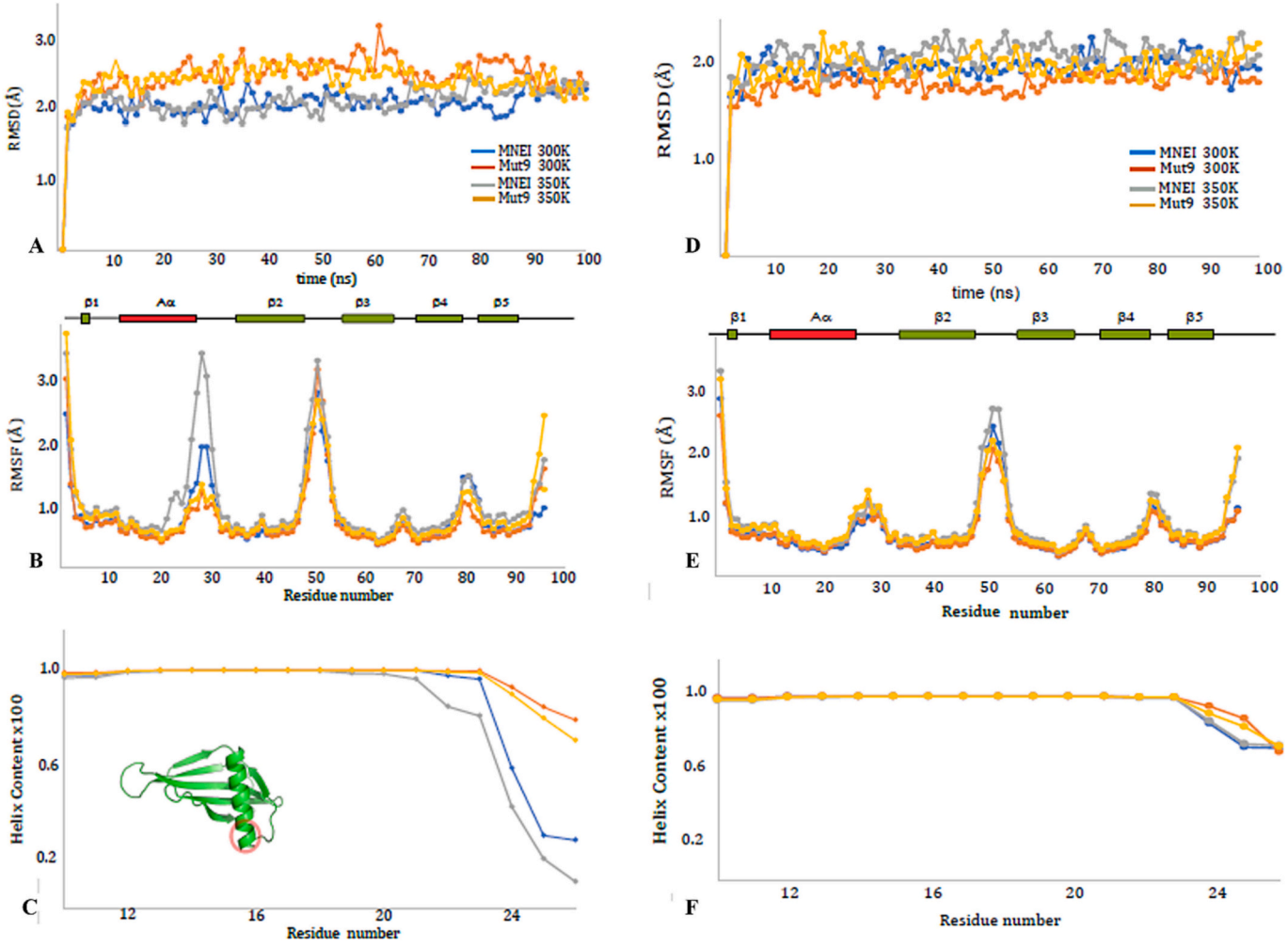

Fig. 8. Molecular dynamics simulations of MNEI and Mut9 at pH 6.8 (panels A-C) and pH 2.5 (panels D-F). RMSD along the trajectory are reported in panels A and D, while RMSF of all the Cα atoms in panels B and D, both collected at 300 K (in blue MNEI and in red Mut9) and at 350 K (in grey MNEI and in orange Mut9). In panels C and F, helical structure variation along the trajectory *versus* residue number are shown at pH 6.8 and pH 2.5. The region that loses the helical structure during the 100 ns trajectory is highlighted with a red circle on MNEI structure in panel C.

3.5. Molecular dynamics

Molecular Dynamics simulations were performed on MNEI and Mut9 at acidic and neutral pH both at 300 and 350 K, to gain insights on the different behaviour of the two proteins in terms of stability and aggregation propensity (Fig. 8).

All MD simulations were performed at 100 ns. The structures of the two proteins stay stable along all the trajectories as shown from the root mean square deviation (RMSD) data at pH 6.8 and 2.5 (Fig. 8A and D). The Cα root-mean square fluctuations (RMSF) of all residues are shown in Fig. 8B and E. At acidic pH the two proteins show a similar behaviour along the trajectory (Fig. 8E); they show the same flexibility at the N and C terminus at the linker loop and the Lα2 loop, the loop connecting the C terminal region of the helix and β2 strand, as well in the region between L45 and the beginning of β5. It is interesting to note that Lα2 loop and β5 strand have been previously indicated as likely hot spots involved in triggering amyloid aggregation [42].

At pH 6.8 (Fig. 8B), MNEI is more flexible than Mut9 in the region of the Lα2 loop and the L45 loop beginning of 5β. From the analysis of the variation of secondary structure during the trajectories, MNEI at the same pH loses more that 50 % of the secondary structure in the C terminal region at 300 and 350 K whereas Mut9 secondary structure is unaffected by the variation of pH and temperature (Figs. 8C and 6F).

4. Discussion

MNEI and its variants are useful and established models to study the structural determinants of proteins sweetness. However, these proteins can be also studied to better understand the molecular basis of the aggregation process which governs protein fibrils formation. In the present work, we have focused the attention on two proteins of this family, MNEI and its mutant Mut9. We have already reported, in a previous work, that Mut9 is a super stable mutant [26], and even sweeter than the parent protein. Here, we showed that MNEI and Mut9 possess a comparable number of hydrogen bonds and salt bridges, similar solvent-accessible surfaces and hidden regions, and similar volume. All these features explain why the two proteins are able to interact with the same receptor, eliciting the sweet taste typical of monellin and its derivatives [26]. Furthermore, by analyzing one by one the mutation sites, we understood why the Y65R substitution in Mut9, responsible of the increased protein sweetness, has a less destabilizing effect than that observed in the Y65R mutant [21], since the additional substitutions introduced in the mutant make its chemical environment more similar to that of MNEI than to that of Y65R. In addition, the E23A and C41A mutations introduce non-polar side chains into two hydrophobic pockets of the protein and eliminate a number of unfavorable interactions observed in MNEI. This procedure is known to stabilize the native structure of proteins by preventing their denaturation. Furthermore, the S76Y mutation allows the formation of hydrogen bonds and van der Waals interactions between tyrosine and the surrounding residues, in particular the formation of hydrogen bonds with residues Lys56 and Asp76. All these interactions contribute to the increase of the thermal stability of Mut9 compared to MNEI.

The increased stability of Mut9 at neutral pH due to the substitution of E23 with alanine provided the possibility to expand the range of conditions to study the fibrillar aggregation process of MNEI and its derivatives. Indeed, using a combination of techniques, here we showed that Mut9 can be converted into fibrils both at acidic and neutral pH, independently from the presence of NaCl. Interestingly, the ionic strength influences the kinetics of aggregation in a different way for the two pH conditions. FTIR analysis indicates that, as in the case of MNEI, at pH 2.5 the presence of NaCl makes the aggregation kinetic faster. In contrast, at neutral pH, the ionic strength slightly delays the process.

TEM data indicate long, less branched fibrils at strong acidic pH (2.5) and without NaCl, *i.e.* at low ionic strength. A possible explanation is that in these conditions the net charge of the protein is positive and, upon partially unfolding, at low ionic strength only limited protein orientations leading to an ordered polymerization exist, making the process slower. Accordingly, the fibril microstructures are more ordered, as indicated by the low absorption at around 1660 cm^{-1} and by the low value of the β-index. High concentrations of NaCl reduce the repulsion between the positively charged side chains on the protein surface, increasing the number of possible relative orientations and accelerating the aggregation process. The resulting fibrils are more branched, as revealed by TEM analysis, and less ordered.

At neutral pH the protein net charge is significantly decreased, as the deprotonation of acidic side chains occur. Under these conditions the influence of the ionic strength on both morphology and microstructure is reduced, as both positive and negative charges are present on the protein surface. Interestingly, less fibrils are observed, probably due to the high incubation temperature necessary to partial unfold the protein and prompt the aggregation. The influence of the ionic strength on the kinetics is less clear in this case. As matter of fact, the effect of salts on protein conformational stability and amyloid formation has been debated in the literature. Stabilization of misfolded forms has been proposed to promote protein fibrillization [43] but, in other cases, it has been shown that ions able to stabilize the protein secondary structure also promote aggregation [44,45]. Also, in this case we observed a lower β-index when the kinetics is slower, allowing a more ordered organization.

Punctual analysis to highlight the regions driving the fibrillar aggregation process of the two proteins has been performed by molecular dynamics. Our data points out that the isolated proteins, *i.e.* MNEI and Mut9, have similar behaviour at acidic pH, and confirm that the regions that in previous works [22] were indicated as possible aggregation hot spots have higher flexibility during the trajectories. On the other hand, different properties appear at neutral pH, as MNEI is more flexible along the trajectory than Mut9 and tends to lose partially the helical structure. The exposure and the partial unfolding of the α-helix structure has been indicated as the trigger of protein aggregation start and may explain the different kinetics at neutral pH of the two proteins. Indeed, in this condition, MNEI quickly aggregates and forms amorphous precipitates instead of ordered fibrils. For Mut9, this process occurs much more slowly favoring the fibers formation. Therefore, the introduction of mutations in Mut9 leads to an increased stability at neutral pH not only of the native state, but also of the early unfolded states, prompting the formation of amyloid fibrils even at neutral pH [46], in contrast to MNEI that at neutral pH does not form ordered fibers.

5. Conclusion

In this work, using a multimethodological approach we have highlighted the structural grounds of another interesting property of Mut9 which, besides the extremely high sweetness and stability, is also able to form fibrils of different morphology and size at different pHs and ionic strength. A careful selection of the experimental conditions allows the driving of the process towards aggregates endowed with different microstructures and morphological features, amenable for further biophysical characterization and suitable for different possible applications. Despite the close similarity with MNEI, Mut9 not only is a better candidate as hypocaloric sugar substitute, but also is a more versatile building block to design nanostructured biomaterials [47,48]. Indeed, MNEI and its derivatives are small proteins, which spontaneously fold *in vitro* to produce functional sweet proteins with high thermal stability. They can be lyophilized and stocked for years also in solution. Moreover, they can be produced and easily purified with high yield, through biotechnological procedures which, when compared to protein extraction either from natural sources or wastes, are scalable, independent on climate and geographic issues and safe for the environment. Production cost at this moment represents a limit since we only work on lab scale. However, we are also confident that they can be significantly reduced in future.

Data bank accession numbers

The coordinates of MNEI and Mut9 have been deposited into the PDB under di accession codes 8Q0S and 8Q0R, respectively.

Declaration of competing interest

The authors declare that they have no known competing financial interests or personal relationships that could have appeared to influence the work reported in this paper.

Data availability

Data will be made available on request.

Acknowledgments

We gratefully acknowledge the Elettra Synchrotron staff for their assistance during data collection and Miss. Antonella Giarra for her help during TEM images collection.

Funding information

This research did not receive any specific grant from funding agencies in the public, commercial, or not-for-profit sectors.

Appendix A. Supplementary data

Additional supporting information are provided as "Supplementary Material" Word file. Supporting information includes tables with the analysis of the structural features of MNEI and Mut9, with a comparison with literature data, details of the mutation sites and of the electron density maps from the X-ray structures, pictures of MNEI and Mut9 crystals and a table summering data collection and refinement statistics. Supplementary data to this article can be found online at https://doi.org/10.1016/j.ijbiomac.2023.127775.

References

[1] M. Jucker, L.C. Walker, Self-propagation of pathogenic protein aggregates in neurodegenerative diseases, Nature 501 (2013) 45–51, https://doi.org/10.1038/nature12481.
[2] C.M. Dobson, The structural basis of protein folding and its links with human disease, Philos. Trans. R. Soc. Lond. B 356 (2001) 133–145, https://doi.org/10.1098/rstb.2000.0758.
[3] D.J. Selkoe, Alzheimer's disease is a synaptic failure, Science 298 (2002) 789–791, https://doi.org/10.1126/science.1074069.
[4] L.C. Serpell, M. Sunde, M.D. Benson, G.A. Tennent, M.B. Pepys, P.E. Fraser, The protofilament substructure of amyloid fibrils11Edited by F. E. Cohen, J. Mol. Biol. 300 (2000) 1033–1039, https://doi.org/10.1006/jmbi.2000.3908.
[5] W. Lohcharoenkal, L. Wang, Y.C. Chen, Y. Rojanasakul, Protein nanoparticles as drug delivery carriers for cancer therapy, Biomed. Res. Int. 2014 (2014) 1–12, https://doi.org/10.1155/2014/180549.
[6] P.-L. Lam, W.-Y. Wong, Z. Bian, C.-H. Chui, R. Gambari, Recent advances in green nanoparticulate systems for drug delivery: efficient delivery and safety concern, Nanomedicine 12 (2017) 357–385, https://doi.org/10.2217/nnm-2016-0305.
[7] H. Jahangirian, E. Ghasemian Lemraski, T.J. Webster, R. Rafiee-Moghaddam, Y. Abdollahi, A review of drug delivery systems based on nanotechnology and green chemistry: green nanomedicine, IJN 12 (2017) 2957–2978, https://doi.org/10.2147/IJN.S127683.
[8] J. Zurdo, J.I. Guijarro, J.L. Jiménez, H.R. Saibil, C.M. Dobson, Dependence on solution conditions of aggregation and amyloid formation by an SH3 domain, J. Mol. Biol. 311 (2001) 325–340, https://doi.org/10.1006/jmbi.2001.4858.
[9] Y. Su, P.-T. Chang, Acidic pH promotes the formation of toxic fibrils from β-amyloid peptide, Brain Res. 893 (2001) 287–291, https://doi.org/10.1016/S0006-8993(00)03322-9.
[10] Y. Kusumoto, A. Lomakin, D.B. Teplow, G.B. Benedek, Temperature dependence of amyloid β-protein fibrillization, Proc. Natl. Acad. Sci. U. S. A. 95 (1998) 12277–12282, https://doi.org/10.1073/pnas.95.21.12277.
[11] C.M. Dobson, Protein folding and misfolding, Nature 426 (2003) 884–890, https://doi.org/10.1038/nature02261.
[12] B. Caughey, P.T. Lansbury, Protofibrils, pores, fibrils, and neurodegeneration: separating the responsible protein aggregates from the innocent bystanders, Annu. Rev. Neurosci. 26 (2003) 267–298, https://doi.org/10.1146/annurev.neuro.26.010302.081142.
[13] G. Bitan, M.D. Kirkitadze, A. Lomakin, S.S. Vollers, G.B. Benedek, D.B. Teplow, Amyloid β-protein (Aβ) assembly: Aβ40 and Aβ42 oligomerize through distinct pathways, Proc. Natl. Acad. Sci. U. S. A. 100 (2003) 330–335, https://doi.org/10.1073/pnas.222681699.
[14] A.P. Pawar, K.F. DuBay, J. Zurdo, F. Chiti, M. Vendruscolo, C.M. Dobson, Prediction of "aggregation-prone" and "aggregation-susceptible" regions in proteins associated with neurodegenerative diseases, J. Mol. Biol. 350 (2005) 379–392, https://doi.org/10.1016/j.jmb.2005.04.016.
[15] N.S. De Groot, I. Pallarés, F.X. Avilés, J. Vendrell, S. Ventura, Prediction of "hot spots" of aggregation in disease-linked polypeptides, BMC Struct. Biol. 5 (2005) 18, https://doi.org/10.1186/1472-6807-5-18.
[16] T. Tancredi, H. Iijima, G. Saviano, P. Amodeo, P.A. Temussi, Structural determination of the active site of a sweet protein a ^{1}H NMR investigation of pMNEI, FEBS Lett. 310 (1992) 27–30, https://doi.org/10.1016/0014-5793(92)81138-C.
[17] T. Kimura, T. Uzawa, K. Ishimori, I. Morishima, S. Takahashi, T. Konno, S. Akiyama, T. Fujisawa, Specific collapse followed by slow hydrogen-bond formation of β-sheet in the folding of single-chain monellin, Proc. Natl. Acad. Sci. U. S. A. 102 (2005) 2748–2753, https://doi.org/10.1073/pnas.0407982102.
[18] A.K. Patra, J.B. Udgaonkar, Characterization of the folding and unfolding reactions of single-chain monellin: evidence for multiple intermediates and competing pathways, Biochemistry 46 (2007) 11727–11743, https://doi.org/10.1021/bi701142a.
[19] A. Kaushik, J.B. Udgaonkar, Replacement of the native cis prolines by alanine simplifies the complex folding mechanism of a small globular protein by eliminating both fast and slow phases of folding, Biophys. J. (2023), S0006349523005271, https://doi.org/10.1016/j.bpj.2023.08.012.
[20] S.K. Jha, J.B. Udgaonkar, Direct evidence for a dry molten globule intermediate during the unfolding of a small protein, Proc. Natl. Acad. Sci. U. S. A. 106 (2009) 12289–12294, https://doi.org/10.1073/pnas.0905744106.
[21] A. Pica, S. Leone, R. Di Girolamo, F. Donnarumma, A. Emendato, M.F. Rega, A. Merlino, D., Picone, pH driven fibrillar aggregation of the super-sweet protein Y65R-MNEI: a step-by-step structural analysis, Biochim. Biophys. Acta Gen. Subj. 1862 (2018) 808–815, https://doi.org/10.1016/j.bbagen.2017.12.012.
[22] F. Donnarumma, S. Leone, M. Delfi, A. Emendato, D. Ami, D.V. Laurents, A. Natalello, R. Spadaccini, D. Picone, Probing structural changes during amyloid aggregation of the sweet protein MNEI, FEBS J. 287 (2020) 2808–2822, https://doi.org/10.1111/febs.15168.
[23] F. Donnarumma, A. Emendato, S. Leone, C. Ercole, G. D'Errico, D. Picone, Salt modulated fibrillar aggregation of the sweet protein MNEI in aqueous solution, J. Solut. Chem. 47 (2018) 939–949, https://doi.org/10.1007/s10953-018-0764-6.
[24] Q. Liu, L. Li, L. Yang, T. Liu, C. Cai, B. Liu, Modification of the sweetness and stability of sweet-tasting protein monellin by gene mutation and protein engineering, Biomed. Res. Int. 2016 (2016) 1–7, https://doi.org/10.1155/2016/3647173.
[25] V. Esposito, R. Gallucci, D. Picone, G. Saviano, T. Tancredi, P.A. Temussi, The importance of electrostatic potential in the interaction of sweet proteins with the sweet taste receptor, J. Mol. Biol. 360 (2006) 448–456, https://doi.org/10.1016/j.jmb.2006.05.020.
[26] M. Delfi, A. Emendato, S. Leone, E.A. Lampitella, P. Porcaro, G. Cardinale, L. Petraccone, D. Picone, A super stable mutant of the plant protein monellin endowed with enhanced sweetness, Life 11 (2021) 236, https://doi.org/10.3390/life11030236.
[27] C. Vonrhein, C. Flensburg, P. Keller, A. Sharff, O. Smart, W. Paciorek, T. Womack, G. Bricogne, Data processing and analysis with the autoPROC toolbox, Acta Crystallogr. D Biol. Crystallogr. 67 (2011) 293–302, https://doi.org/10.1107/S0907444911007773.
[28] G.N. Murshudov, P. Skubák, A.A. Lebedev, N.S. Pannu, R.A. Steiner, R.A. Nicholls, M.D. Winn, F. Long, A.A. Vagin, REFMAC 5 for the refinement of macromolecular crystal structures, Acta Crystallogr. D Biol. Crystallogr. 67 (2011) 355–367, https://doi.org/10.1107/S0907444911001314.
[29] P. Emsley, B. Lohkamp, W.G. Scott, K. Cowtan, Features and development of coot, Acta Crystallogr. D Biol. Crystallogr. 66 (2010) 486–501, https://doi.org/10.1107/S0907444910007493.
[30] M. Delfi, S. Leone, A. Emendato, D. Ami, M. Borriello, A. Natalello, C. Iannuzzi, D. Picone, Understanding the self-assembly pathways of a single chain variant of monellin: a first step towards the design of sweet nanomaterials, Int. J. Biol. Macromol. 152 (2020) 21–29, https://doi.org/10.1016/j.ijbiomac.2020.02.229.
[31] D.A. Case, K. Belfon, I.Y. Ben-Shalom, S.R. Brozell, D.S. Cerutti, T.E. Cheatham III, V.W.D. Cruzeiro, T.A. Darden, R.E. Duke, G. Giambasu, M.K. Gilson, H. Gohlke, A. W. Goetz, R. Harris, S. Izadi, S.A. Izmailov, K. Kasavajhala, A. Kovalenko, R. Krasny, T. Kurtzman, T.S. Lee, S. LeGrand, P. Li, C. Lin, J. Liu, T. Luchko, R. Luo, V. Man, K.M. Merz, Y. Miao, O. Mikhailovskii, H. Nguyen, G. M., A. Onufriev, F. Pan, S. Pantano, R. Qi, D.R. Roe, A. Roitberg, C. Sagui, S. Schott-Verdugo, J. Shen, C.L. Simmerling, N.R. Skrynnikov, J. Smith, J. Swails, R.C. Walker, J. Wang, L. Wilson, R.M. Wolf, X. Wu, Y. Xiong, Y. Xue, D.M. York, P.A. Kollman, Amber 2020, University of California, San Francisco, n.d.
[32] R. Anandakrishnan, B. Aguilar, A.V. Onufriev, H++ 3.0: automating pK prediction and the preparation of biomolecular structures for atomistic molecular modeling and simulations, Nucleic Acids Res. 40 (2012) W537–W541, https://doi.org/10.1093/nar/gks375.
[33] D.R. Roe, T.E. Cheatham, PTRAJ and CPPTRAJ: software for processing and analysis of molecular dynamics trajectory data, J. Chem. Theory Comput. 9 (2013) 3084–3095, https://doi.org/10.1021/ct400341p.

[34] H. Nguyen, D.A. Case, A.S. Rose, NGLview–interactive molecular graphics for Jupyter notebooks, Bioinformatics 34 (2018) 1241–1242, https://doi.org/10.1093/bioinformatics/btx789.
[35] Z. Sun, Q. Liu, G. Qu, Y. Feng, M.T. Reetz, Utility of B-factors in protein science: interpreting rigidity, flexibility, and internal motion and engineering thermostability, Chem. Rev. 119 (2019) 1626–1665, https://doi.org/10.1021/acs.chemrev.8b00290.
[36] V. Esposito, R. Gallucci, D. Picone, G. Saviano, T. Tancredi, P.A. Temussi, The importance of electrostatic potential in the interaction of sweet proteins with the sweet taste receptor, J. Mol. Biol. 360 (2006) 448–456, https://doi.org/10.1016/j.jmb.2006.05.020.
[37] W. Zheng, L. Yang, C. Cai, J. Ni, B. Liu, Expression, purification and characterization of a novel double-sites mutant of the single-chain sweet-tasting protein monellin (MNEI) with both improved sweetness and stability, Protein Expr. Purif. 143 (2018) 52–56, https://doi.org/10.1016/j.pep.2017.10.010.
[38] T. Weiffert, S. Linse, Protein stabilization with retained function of monellin using a split GFP system, Sci. Rep. 8 (2018) 12763, https://doi.org/10.1038/s41598-018-31177-z.
[39] N. Aghera, I. Dasgupta, J.B. Udgaonkar, A buried ionizable residue destabilizes the native state and the transition state in the folding of monellin, Biochemistry 51 (2012) 9058–9066, https://doi.org/10.1021/bi3008017.
[40] F. Chiti, C.M. Dobson, Protein misfolding, amyloid formation, and human disease: a summary of progress over the last decade, Annu. Rev. Biochem. 86 (2017) 27–68, https://doi.org/10.1146/annurev-biochem-061516-045115.
[41] R. Sarroukh, E. Goormaghtigh, J.-M. Ruysschaert, V. Raussens, ATR-FTIR: a "rejuvenated" tool to investigate amyloid proteins, Biochim. Biophys. Acta Biomembr. 1828 (2013) 2328–2338, https://doi.org/10.1016/j.bbamem.2013.04.012.
[42] Y. Yoshimura, Y. Lin, H. Yagi, Y.-H. Lee, H. Kitayama, K. Sakurai, M. So, H. Ogi, H. Naiki, Y. Goto, Distinguishing crystal-like amyloid fibrils and glass-like amorphous aggregates from their kinetics of formation, Proc. Natl. Acad. Sci. U. S. A. 109 (2012) 14446–14451, https://doi.org/10.1073/pnas.1208228109.
[43] D.-S. Yang, C.M. Yip, T.H.J. Huang, A. Chakrabartty, P.E. Fraser, Manipulating the amyloid-β aggregation pathway with chemical chaperones, J. Biol. Chem. 274 (1999) 32970–32974, https://doi.org/10.1074/jbc.274.46.32970.
[44] P. Arosio, B. Jaquet, H. Wu, M. Morbidelli, On the role of salt type and concentration on the stability behavior of a monoclonal antibody solution, Biophys. Chem. 168–169 (2012) 19–27, https://doi.org/10.1016/j.bpc.2012.05.004.
[45] L.A. Sikkink, M. Ramirez-Alvarado, Salts enhance both protein stability and amyloid formation of an immunoglobulin light chain, Biophys. Chem. 135 (2008) 25–31, https://doi.org/10.1016/j.bpc.2008.02.019.
[46] A.W. Fitzpatrick, T.P.J. Knowles, C.A. Waudby, M. Vendruscolo, C.M. Dobson, Inversion of the balance between hydrophobic and hydrogen bonding interactions in protein folding and aggregation, PLoS Comput. Biol. 7 (2011), e1002169, https://doi.org/10.1371/journal.pcbi.1002169.
[47] G. Wei, Z. Su, N.P. Reynolds, P. Arosio, I.W. Hamley, E. Gazit, R. Mezzenga, Self-assembling peptide and protein amyloids: from structure to tailored function in nanotechnology, Chem. Soc. Rev. 46 (2017) 4661–4708, https://doi.org/10.1039/C6CS00542J.
[48] M. Peydayesh, J. Vogt, X. Chen, J. Zhou, F. Donat, M. Bagnani, C.R. Müller, R. Mezzenga, Amyloid-based carbon aerogels for water purification, Chem. Eng. J. 449 (2022), 137703, https://doi.org/10.1016/j.cej.2022.137703.